



Machine learning in multiscale modeling of spatially tailored materials with microstructure uncertainties



Shaoping Xiao ^{a,*}, Phillip Deierling ^b, Siamak Attarian ^c, Ahmed El Tuhami ^b

^a Department of Mechanical Engineering, Iowa Technology Institute, 3131 Seamans Center, The University of Iowa, Iowa City, IA 52242, United States

^b Department of Mechanical Engineering, The University of Iowa, Iowa City, IA 52242, United States

^c Department of Mechanical Engineering, Iowa Technology Institute, The University of Iowa, Iowa City, IA 52242, United States

ARTICLE INFO

Article history:

Received 10 June 2020

Accepted 13 February 2021

Available online 18 March 2021

Keywords:

Machine learning

Neural network

Multiscale

Composites

Microstructure uncertainty

ABSTRACT

In this paper, a novel hierarchical micro–macro multiscale modeling enhanced via machine learning is proposed. Machine learning plays an important role in this multiscale framework to pass the information from the microscale to the macroscale. This multiscale method provides a new approach to study the mechanics of a metal–ceramic ($Ti-TiB_2$) spatially tailored material in which the volume fractions vary in space at the macroscale. Data sets, collected from microscale simulations, are used to train machine learning regression and classification models. Those predictive models are then implemented in the macroscale simulations to study dynamical responses of spatially tailored $Ti-TiB_2$ structures under various loading conditions. As a difference from other reported works, microstructure uncertainties are considered in this paper so that an artificial neural network is trained as the machine learning classification model to predict the failure probability at the macroscale, which depends on the volume fraction and the deformation (i.e., the strain).

Published by Elsevier Ltd.

1. Introduction

Riding the wave of artificial intelligence (AI), machine learning (ML) and deep learning (DL) methods have been widely used in many domains, including materials science and engineering [1]. For instance, ML potential functions [2] have been employed for atomistic simulations. In contrast to employing empirical potential functions, this alternative approach uses ML to represent potential-energy surfaces by fitting large data sets, which were collected from electronic structure calculations. On the other hand, there were quite a few achievements in using artificial neural networks (ANNs) to learn complex constitutive relationships in continuum simulations. Stoffel et al. [3,4] applied intelligent finite element methods (FEMs) in nonlinear structural mechanics. They used an empirical constitutive relation to generate the training data, with which an ANN was trained and employed in FEMs. Back-propagation ANNs [5–7] were also used to approximate constitutive modeling at various strain rates and high temperatures. In addition, Freitag and co-workers [8] used a recurrent neural network (RNN) to describe time-dependent material behaviors in FEMs. Some ML/DL applications in computational mechanics [9] include accelerating total Lagrangian explicit dynamics [10], solv-

ing eigenvalue problems in mechanics [11], developing smart FEM [12], and generating material performance databases [13].

Machine learning has also been used in other research in the domain of materials science. In modeling and simulation of manufacturing, Esmailzadeh and Aghaie-Khafri [14] used FEM and ANN to simulate Equal Channel Angular Pressing (ECAP) deformation of AA2024 aluminum alloy, and the results were found to be in good agreement with experimental measurements. Fu et al. [15] used a genetic algorithm (GA) to optimize the weights of ANNs, which were taken as a new approach for punch and process design of air-bending forming of metal sheets. PourAsabi et al. [16] used experimental results to train a multi-layer perceptron (MLP) model for estimating the Vickers hardness of alloys after the austempering treatment. To study material corrosion, Kappatos et al. [17] used an ANN with a radial basis function to assess the effect of existing corrosion damage on the residual tensile properties of alloys. In another work, Birbilis et al. [18] developed an ANN model to predict the corrosion rate and the yield strength of magnesium–rare earth alloys. Recently, Anitescu et al. [19] and Samaniego et al. [20] utilized the energy of a mechanical system as the loss function of ANNs to solve partial differential equations via an adaptive collocation strategy.

As a powerful numerical tool, multiscale modeling has been utilized in studying various physical phenomena at different scales. In concurrent multiscale methods [21–24], various length/time scales

* Corresponding author.

E-mail address: shaoping-xiao@uiowa.edu (S. Xiao).

are coupled, and simulations are conducted simultaneously. Talebi et al. [73] employed the bridging domain method to couple the three-dimensional extended finite element method (XFEM) with molecular dynamics (MD) to simulate crack propagation in dynamics. They also applied this concurrent multiscale framework to studies of material failure in nanocomposites [74,75]. By contrast, hierarchical multiscale methods conduct simulations at different scales one by one. One approach to pass information from one scale to another in hierarchical multiscale modeling is the homogenization technique, named the Cauchy-Born rule [25,26], in which the constitutive relations for continuum simulations are analytically derived based on the molecular potential. Such a homogenization technique has been extended to the exponential Cauchy-Born rule [27] and the temperature-related Cauchy-Born rule [28–30]. Another approach to bridge the scales is to conduct molecular dynamics (MD) simulations to estimate material properties, which are then passed to continuum simulations. For example, the friction coefficient between sliding solids [31] was calculated via MD and then was passed to FEM simulations to study the rolling contact fatigue [32]. In another work, Jiang et al. [33] used MD simulations to construct an elasto-damage model, which was used in material point methods for large-scale simulations.

Recently, multiscale modeling and simulation have benefited from ML and DL [34]. Unger and Könke [35] adopted ANN in a multiscale approach to study reinforced concrete beams. In their approach, the data set, obtained from mesoscale simulations, was used to train ANNs to predict tangential stresses in macroscale simulations. Liu et al. [36] developed a new data-driven multiscale method, i.e., a deep material network, to describe complex overall material responses of heterogeneously structured composites. White and co-workers [37] used a single-layer feedforward neural network as a surrogate model to predict the elastic response of the microscale metamaterial. They employed this surrogate model to conduct optimization of macroscale elastic structures. In addition, Lu et al. [38] conducted work to simulate the macroscale dynamics of gas-solid mixtures by employing information collected from microscale simulations via an ANN model. Recently, Xiao et al. [39] proposed a machine-learning-enhanced hierarchical multiscale framework. In their approach, the data sets collected from MD were used to train machine learning regression and classification models, which were then implemented in continuum simulations at the macroscale. Other recent achievements include a multiscale multi-permeability poroplasticity model [40], a 3D architecture of deep material network [41], and neural network-assisted multiscale analysis [42].

Spatially tailored materials (STMs) [43], also named functionally graded materials (FGMs), are one of the next-generation composites for use in multi-physical problems. STMs are essentially composites consisting of two or more phases of distinct materials in which the volume fractions continuously change in space. This unique class of heterogeneous composites offers advantages over traditional composites due to its ability to leverage the predominant characteristics of the constituent materials and to tailor the effective material properties according to the loading conditions and operating temperatures. Many experimental works have been done on metal-ceramic STMs, including Ti-TiB₂ STMs. Patil et al. [44] investigated direct metal laser sintering (DMLS) processed Ti-6Al-4V alloy with the addition of varying amounts of TiB₂. They observed that the microstructure changed from a martensite lath to a refined bimodal structure with the increased weight fraction of TiB₂. As a result, hardness and wear performance were dramatically improved. In their microstructure images, the spots of porosity were clearly visible and resulted in 1–2% reduction in the material density. Shishkovsky et al. [45] utilized selective laser melting to fabricate graded layered Ti matrix composite with TiB₂ inclusions. After investigating the microstructure via SEM,

they identified two types of heterogeneity. In addition, Cai and co-workers [46] prepared in situ synthesized TiB/Ti-6Al-4V nanocomposites via laser additive manufacturing and investigated the effects of reinforcement content on microstructure and mechanical properties. They found that the composite nano-hardness was much higher than traditionally sintered composites.

Current standard practice for numerical modeling of STMs involves using principles of micromechanics [47–49], such as analytical modeling and numerical homogenization of representative volume elements (RVEs), to bridge the gap to the macroscale. Deierling and Zhupanska [50] developed a holistic computational framework for modeling the highly nonlinear coupled thermomechanical response of spatially tailored metal-ceramic structures subjected to combined thermal and mechanical loads. In this model, the effective spatially varying material properties of graded microstructures over a wide temperature range were estimated using numerical homogenization of RVEs based on FEM simulations. However, most of those practices ignored the uncertainties of the composite microstructure, which should be considered to accurately predict material responses at the macroscale.

In this paper, we propose a hierarchical multiscale method to study the mechanics of spatially tailored Ti-TiB₂ structures. The contribution highlights of this work include the following: (1) Microstructure uncertainties, including particle number, size, shape, and location, are considered during data collection via microscale simulations. Previous works [47–50], however, didn't consider uncertainties when estimating effective material properties at the microscale. (2) The proposed multiscale modeling of STMs utilizes ML to pass messages from microscale to macroscale. Microscale simulations are conducted to generate the data sets, which are used to train the ML regression and classification models. Then, well-trained machines are implemented in macroscale simulations. Specifically, a neural network-based classification model is trained to predict the material failure probability at the macroscale. This is different from one of the author's prior achievements [39,51], in which material failure was deterministically predicted via neural networks. Also, the work in [39] and [51] utilized ML models to pass messages from nanoscale to macroscale without the consideration of uncertainties, and it cannot directly apply for studies of STMs.

The outline of this paper is described as follows. After the introduction, Ti-TiB₂ STMs and the microstructure uncertainties are described in Section 2. Section 3 includes a description of microscale simulations and data collection. The proposed hierarchical multiscale method and machine learning models are narrated in Section 4. Macroscale simulations of spatially tailored Ti-TiB₂ structures with the implementation of machine learning predictive models are discussed in Section 5, followed by conclusions and future outlook in Section 6.

2. Metal-ceramic spatially tailored materials and microstructures

2.1. Ti-TiB₂ spatially tailored materials

The metal-ceramic STMs studied in this paper are Ti-TiB₂ composites with the volume fractions varying in space. The material properties of Ti and TiB₂ are listed in Table 1 according to references [52–54]. Only the room temperature (20 °C) is considered in this paper.

It is common for STMs to be modeled as continuously variable composition materials. We use the ceramic volume fraction (CVF) to represent the difference of two materials, i.e., metal (Ti) and ceramic (TiB₂), at a particular spatial location. It is obvious that the metal (Ti) is the matrix material when the CVF is less than

Table 1

Material properties of Ti (Ti-6Al-4V) and TiB₂ at 20 °C.

	Young's modulus E (GPa)	Poisson's ratio ν	Density ρ (kg/m ³)	Tensile strength σ_t (GPa)
Ti (Ti-6Al-4V)	106.2	0.298	4357	1.17
TiB ₂	495.4	0.100	4505	3.73

50%, while the ceramic (TiB₂) is the matrix material when the CVF is larger than 50%.

Considering a plate made of Ti-TiB₂ in which the volume fractions vary along with the thickness, the CVF, ν_f , is determined via a power-law distribution,

$$\nu_f(z) = \nu_0 + (\nu_1 - \nu_0) \left(\frac{z}{h} \right)^n \quad (1)$$

where z is the thickness coordinate, and h is the total thickness. ν_0 and ν_1 are the CVFs at two surfaces where $z = 0$ and $z = h$, respectively. It is assumed that $\nu_0 = 0$ and $\nu_1 = 1.0$ in our simulations. In addition to ν_0 and ν_1 , n is another parameter to control the ceramic content. We choose $n = 1$ for the linear distribution and $n = 2$ (quadratic) or 0.5 (square root) for the nonlinear distributions. Fig. 1 illustrates the numeric changes of CVF along with the thickness via three different distributions, while Fig. 2 includes artificially generated images to demonstrate the content changes of Ti (represented via white) and TiB₂ (represented via black).

In addition, more than one directional material variation is permissible. For example, in the case of two-directional graded materials, the CVF can be prescribed by the following:

$$\nu_f(x, z) = \nu_0 + (\nu_1 - \nu_0) \left[\eta_x \left(\frac{x}{w} \right)^{n_x} + \eta_z \left(\frac{z}{h} \right)^{n_z} \right] \quad (2)$$

where x and z are the coordinates in the horizontal and vertical directions, w and h are the total width and height, and η_i and n_i are parameters controlling the ceramic content and profile in each direction, respectively, while ν_0 and ν_1 are the minimum and maximum CVFs. Similar to the one-directional material variation case described in Eq. (1), $\nu_0 = 0$ and $\nu_1 = 1.0$ are assumed in Eq. (2) in this paper. Fig. 3 shows the contours of CVFs in a 2D plate when two control parameters, n_x and n_z in Eq. (2), are assigned with different values while $\eta_x = \eta_z = 0.5$.

2.2. Microstructure uncertainties

To study the mechanics of STMs, which are heterogeneous material at the macroscale, the local mechanical behaviors, including the stress-strain relations and failure occurrences at various material points, need to be investigated first via microscale simu-

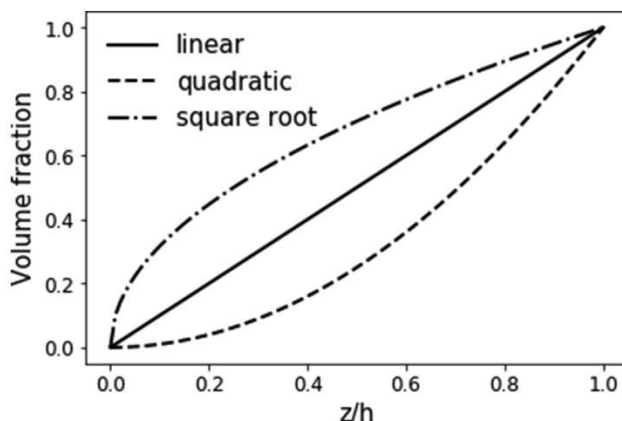
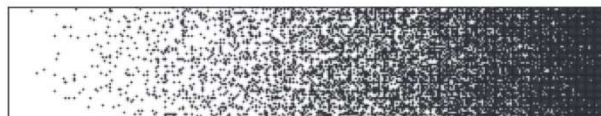


Fig. 1. The CVF distributions along with the thickness.



(a) linear distribution



(b) quadratic distribution



(c) square root distribution

Fig. 2. Artificially generated images of STMs with different CVF distributions.

lations. According to the spatial coordinates of a material point, the CVF can be determined via Eqs. (1) or (2). At each material point, the CVF is assumed to be a constant at the microscale. However, the microstructures may vary at different material points although the CVFs are the same at those locations.

A few microstructure uncertainties related to the inclusion particles (either ceramic or metal particles depending on whether or not the CVF is less than 50%) are considered when conducting microscale simulations to collect data. Those microstructure uncertainties include the number of particles, the particle location, the particle shape, and the particle size. In this paper, we employ a homogenous Poisson point process [55] to determine the number of Poisson points, i.e., the number of inclusion particles, in a finite two-dimensional plane at a prescribed particle volume fraction. The probability of the number (k) of Poisson points (i.e., particles) can be written as:

$$P(k) = \frac{e^{-\lambda A} (\lambda A)^k}{k!}, \quad k = 1, 2, 3, \dots \quad (3)$$

where A is the plane area, and λ is the Poisson point density, i.e., the particle density, per area.

During the Ti-TiB₂ STM manufacturing processing [56], the average particle sizes were 0.76 μm (Ti powder) and 0.54 μm (TiB₂ powder) after ball milling. Therefore, in a 5 μm × 5 μm specimen with 10% CVF, the density of the TiB₂ ceramic particle is 0.53/μm². As a result, the probability of the number of TiB₂ particles can be determined via Eq. (3) and is shown in Fig. 4. It can be seen that the number of particles is in the range of 5–23, and each number of particles has its own probability of occurrence. For instance, the occurrence probability of 13 TiB₂ particles in the specimen is 11%. In other words, if 100 computational samples are chosen to study the mechanical behaviors of composites with 10% TiB₂ (by volume), there shall be eleven microstructure samples containing 13 TiB₂ particles.

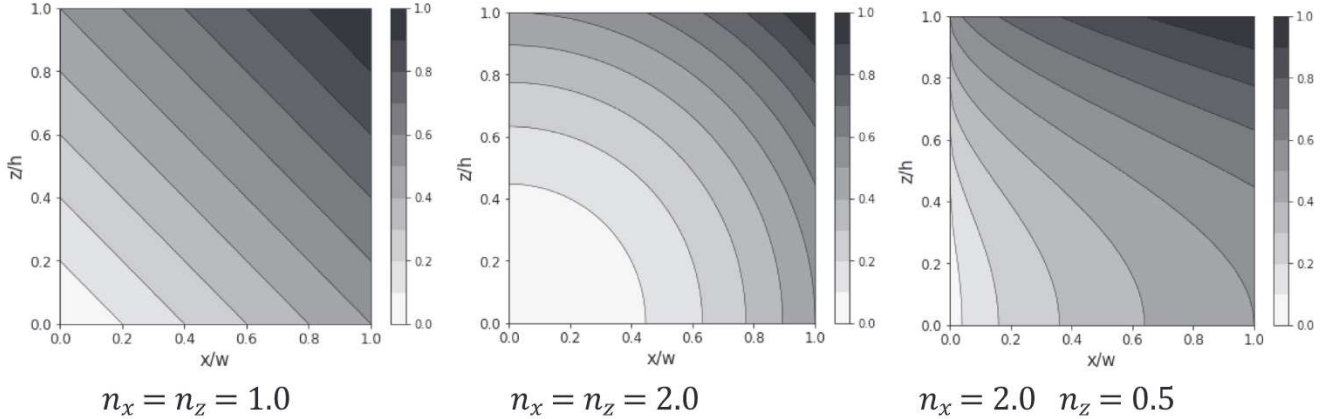


Fig. 3. The contours of CVF distributions in 2D STM plates.

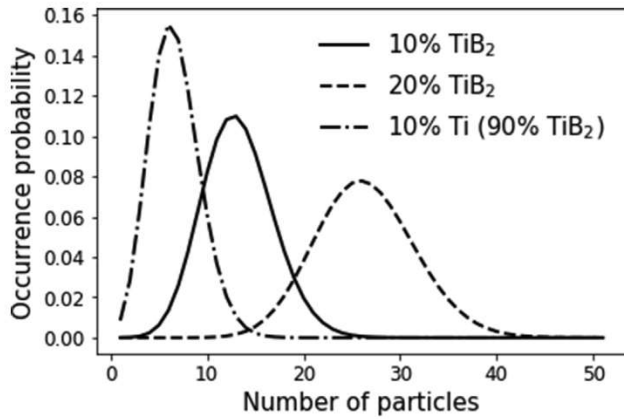


Fig. 4. Occurrence probabilities of the number of particles.

It shall be noted that the average sizes of Ti and TiB₂ powders were different from the previous report [56]. Therefore, the occurrence probability of the number of Ti particles at the metal volume fraction of 10% (i.e., 90% CVF) is different from the probability of the number of TiB₂ particles at 10% CVF. In addition to the number of particles, the locations of particles are randomly assigned in the simulation domain. Polygons with four to eight edges are considered as various shapes of particles. The sizes of particles are randomly chosen within the variation of $\pm 50\%$ of the average particle size. Fig. 5 illustrates a few microstructure samples that are randomly generated when the CVF is 20%.

As the volume fraction increases, it is possible for the neighboring particles to form a big particle or a cluster. In addition, pores were usually observed in SEM images of metal-ceramic STMs [45,57]. In this paper, our simulations are conducted for the composites with CVFs from 1% to 25% and from 75% to 99% so that only individual particles are considered in the microstructure configurations without porosity. The material properties at the CVFs between 25% and 75% are expected to be obtained via machine learning regression models. In future research, we will employ advanced mesh generation techniques to generate microstructure configurations with clusters and pores at the intermediate CVFs.

3. Microscale simulations and data collection

3.1. Finite element analysis

The physical principles governing the continuum in solids are the conservation of mass, momentum, and energy. Continuum mechanics is assumed at both microscale and macroscale in this paper. Since the metal-ceramic composites exhibit elasticity with small deformations, we consider a Lagrangian description under adiabatic conditions. Therefore, the conservation of linear momentum equations [58] can be written as

$$\rho \ddot{u}_i = \frac{\partial \sigma_{ji}}{\partial x_j} + \rho b_i \quad (4)$$

where ρ is the density, σ is the stress tensor, b is the body force per unit mass, u is the displacement, and the superposed dots represent material time derivatives. It shall be noted that i and j can be 1, 2, or 3 for a general three-dimensional problem. Eq. (4) with proper

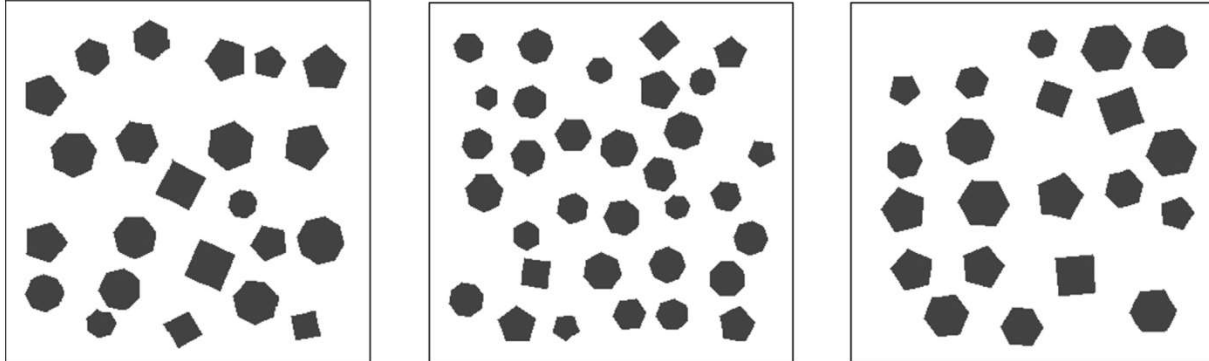


Fig. 5. Microstructure configurations at 20% CVF.

boundary conditions is called the strong form, which can be transferred to the weak form by taking the product of the momentum equations with the test function, δu_i , and integrating over the solution domain, Ω . This gives

$$\int_{\Omega} \delta u_i \rho \ddot{u}_i d\Omega = \int_{\Omega} \delta u_i \rho b_i d\Omega - \int_{\Omega} \frac{\partial(\delta u_i)}{\partial x_j} \sigma_{ji} d\Omega + \int_{\Gamma} \delta u_i \bar{t}_i d\Gamma \quad (5)$$

where \bar{t}_i is the prescribed boundary traction on the boundary Γ .

In this paper, both microscale and macroscale simulations are conducted via FEM methods. Fig. 6 shows that the solution domain of a microscale specimen is discretized into a number of elements and nodes for FEM simulations. The displacement field in each element can be approximated by nodal displacements via the FEM interpolation

$$u_i(\mathbf{x}, t) = \sum_I N_I(\mathbf{x}) u_{ii}(t) \quad (6)$$

where $u_{ii}(t)$ is the i th component of displacement at node I while $N_I(\mathbf{x})$ is the shape function (also called the interpolation function) associated with node I . Linear elements, including two-node bar elements and three-node triangular elements, are adopted in this paper so that the strain tensor in each element is constant and can be calculated as

$$\varepsilon_{ij} = \frac{1}{2} \left(\frac{\partial u_i}{\partial x_j} + \frac{\partial u_j}{\partial x_i} \right) = \frac{1}{2} \left(\sum_I \frac{\partial N_I(\mathbf{x})}{\partial x_j} u_{ii}(t) + \sum_I \frac{\partial N_I(\mathbf{x})}{\partial x_i} u_{jj}(t) \right) \quad (7)$$

Substituting Eq. (6) into the weak form, i.e., Eq. (5), the following discrete equations are obtained:

$$m_I \ddot{u}_{ii} = f_{ii}^{\text{ext}} - f_{ii}^{\text{int}} \quad (8)$$

where $m_I = \rho V_I$ in which V_I is the volume associated with node I . f_{ii}^{ext} and f_{ii}^{int} are the external and internal nodal forces, respectively, given by

$$f_{ii}^{\text{ext}} = \int_{\Omega} \rho N_I b_i d\Omega + \int_{\Gamma} N_I \bar{t}_i d\Gamma \quad (9)$$

$$f_{ii}^{\text{int}} = \int_{\Omega} \frac{\partial N_I(\mathbf{x})}{\partial x_j} \sigma_{ji} d\Omega \quad (10)$$

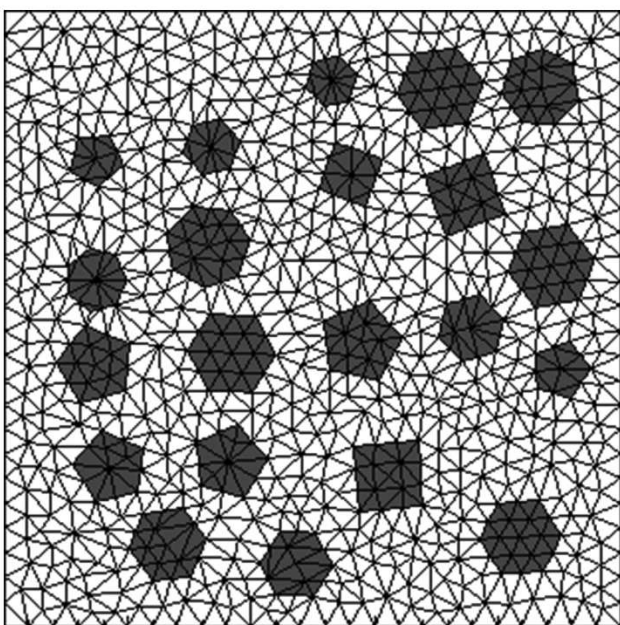


Fig. 6. FEM model of metal-ceramic composites at the microscale.

Based on the theory of elasticity, the constitutive relation in a plane stress state can be written as

$$\begin{Bmatrix} \sigma_x \\ \sigma_y \\ \sigma_{xy} \end{Bmatrix} = \frac{E}{1-\nu^2} \begin{bmatrix} 1 & \nu & 0 \\ \nu & 1 & 0 \\ 0 & 0 & 1-\nu \end{bmatrix} \begin{Bmatrix} \varepsilon_x \\ \varepsilon_y \\ \varepsilon_{xy} \end{Bmatrix} \quad (11)$$

where E is Young's modulus, and ν is Poisson's ratio. In microscale simulations, failure occurs in an element once the element principal stress exceeds the tensile strength, given in Table 1.

The procedure of FEM simulations at the microscale is summarized below:

- (a) Initialize the simulation domain and the boundary/initial conditions.
- (b) Calculate the nodal forces via Eqs. (9) and (10).
- (c) Solve the discrete equations, Eq. (8), to update nodal kinematics.
- (d) Evaluate the element strains based on the FEM approximation via Eq. (7).
- (e) Calculate the element stresses via the constitutive relation, i.e., Eq. (11).
- (f) Determine the material failure/non-failure at each element.
- (g) Repeat (b)–(f) until the simulation is finished.

3.2. Microscale simulations

The purpose of microscale simulations is to generate the data sets representing: (1) the relations between material properties and the CVF; and (2) the failure occurrence depending on the CVF and the subjected deformation. The data sets will be used to train ML regression and classification models for macroscale simulations. In this paper, we consider $5 \mu\text{m} \times 5 \mu\text{m}$ RVEs under the uniaxial tension via the prescribed displacement applied on the top while the bottom is fixed. The FEM method with linear triangular elements is employed. A low strain rate is maintained so that the quasi-static analyses can be approximated by the conducted dynamic simulations. At each simulation, the effective stress-strain relationship is recorded. The volume-averaged stress and strain over the whole solution domain are calculated as the effective stress and strain, shown as

$$\sigma_{\text{eff}} = \frac{1}{V} \sum_I \sigma_I V_I, \quad \varepsilon_{\text{eff}} = \frac{1}{V} \sum_I \varepsilon_I V_I \quad (12)$$

where V is the total volume of the simulation domain, and σ_I and ε_I are the element stress and strain tensors, respectively, at element I with the volume of V_I . Consequently, Young's modulus can be calculated by $\sigma_{\text{eff}}/\varepsilon_{\text{eff}}$ in the vertical direction. In addition, Poisson's ratio is determined via the ratio of horizontal to vertical effective strain.

Microscale simulations with randomly generated microstructure configurations are conducted. At first, Ti-TiB₂ composites with two different CVFs, 10% and 20%, are studied to investigate the variations of material properties due to the microstructure uncertainties. At each CVF, 100 microstructure configurations are randomly generated so that 100 simulations are conducted. The material properties, including Young's modulus, Poisson's ratio, and the tensile strength, are calculated according to the effective stress-strain relation resulting from each simulation.

Fig. 7 illustrates the effective stress-strain relations from three individual simulations of Ti-TiB₂ composites with 20% CVF. It can be seen that the composites exhibit elastic behaviors and that the effective stress-strain relations are almost identical unless the failures occur at different strains. In our simulations, if the principal stress of an element exceeds the material tensile strength, the material failure occurs at this element, and the crack

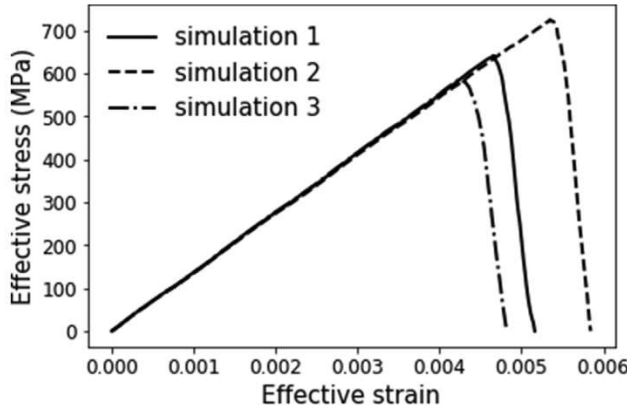


Fig. 7. Effective strain–stress relations at 20% CVF.

initiates or propagates via simply deleting the element. Because of the microstructure uncertainties, the crack initiation location and the crack propagation profile vary in different simulations, as shown in Fig. 8.

3.3. Data collection and pre-analyses

Fig. 9 demonstrates the histograms of calculated Young's modulus and tensile strength based on 100 microscale simulations of Ti-TiB₂ composites with the CVF of 20%. It can be seen that both Young's modulus and the tensile strength follow normal distributions. However, the tensile strength has much higher variability than Young's modulus. The coefficient of variation of the tensile strength is 7.6%, while the coefficient of variation of Young's modulus is only 1.04%. We also conduct 100 microscale simulations of Ti-TiB₂ composites with the CVF of 10% and investigate the distributions of Young's modulus and the tensile strength. The same conclusion is reached.

To collect data at the microscale for ML model training, 25 simulations of composites with randomly generated microstructure configurations are conducted at each CVF from 1% to 25% and from 75% to 99% at 1% increments. Young's modulus, Poisson's ratio, and the tensile strength are calculated at each simulation so that there are a total of 1250 collected data samples, in which the CVF is the input variable (i.e., the feature), while the material properties are the output targets. There are a few commonly used analytical formulas [59–61] to predict material properties of composites. Voigt [59] is typically credited with the earliest study of the effective mechanical properties of composite materials by assuming a uniform strain field to average the elastic tensor. Reuss [60] used a

similar approach to estimate the effective compliance tensor of composite materials. In addition, Hashin and Shtrikman [61] (H-S) proposed tighter bounds of elastic properties of composites based on variational principles of the strain energy. Our simulated Young's modulus and Poisson's ratio fall in the range of those analytical solutions, as shown in Fig. 10, in which H-S⁺ and H-S⁻ represent the upper and lower H-S bounds, respectively.

Fig. 11 shows the tensile strength in terms of the CVF. As concluded above, the tensile strength has much higher variability than Young's modulus and Poisson's ratio. Indeed, the failure occurrences of composites with prescribed CVFs at the microscale are not deterministic due to the microstructure uncertainties. We use another approach to illustrate the probability of failure occurrence in a CVF-strain space. At each CVF, according to the strain-stress histories of 25 microscale simulations, the probability of failure occurrence can be calculated at any strain. Considering the CVFs at which all the simulations have been conducted, a binary map that represents failure probability in the CVF-strain space can be plotted. In the “binary” map shown in Fig. 12, the “white” portion represents 100% failure probability, while the black portion represents 100% non-failure probability (i.e., 100% reliability). It can be seen that there is no clear decision boundary to distinguish failure/non-failure domains, but rather a fuzzy interface. Correspondingly, a total of 162,500 data samples are collected; the features of this data set include the CVF and the strain, while the output target is the failure probability.

4. Hierarchical multiscale modeling and machine learning

4.1. Machine-learning-enhanced hierarchical multiscale modeling

We propose a microscale-macroscale hierarchical multiscale method, as depicted in Fig. 13, to study spatially tailored Ti-TiB₂ structures in this paper. In this multiscale framework, microscale simulations are conducted to generate data sets, as described in Section 3, which are then used to train ML models. Two regression models are trained to predict Young's modulus and Poisson's ratio, respectively, based on the composite volume fraction distribution at the beginning of macroscale simulations. In addition, one classification model is trained to predict the material failure probability, and it is implemented in macroscale simulations to replace the failure criterion at each iteration. As a result, the message-passing between microscale and macroscale is enhanced via ML.

The ML models we use in this paper include support vector machines (SVMs), Gaussian processes regression, and ANNs. SVMs [62–64] are one of the popular ML tools for both regression and classification. The estimated output in an SVM nonlinear regression algorithm can be written as

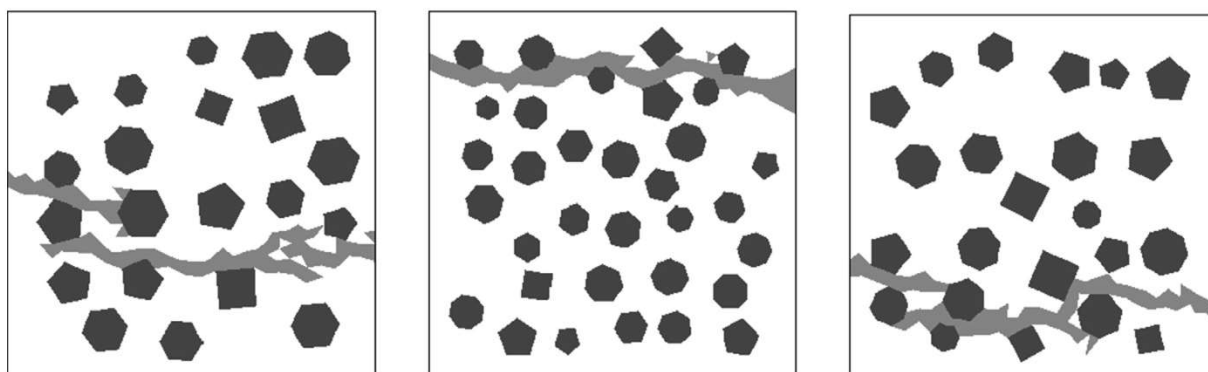


Fig. 8. Microstructure configurations (after failure) of Ti-TiB₂ composites with 20% CVF.

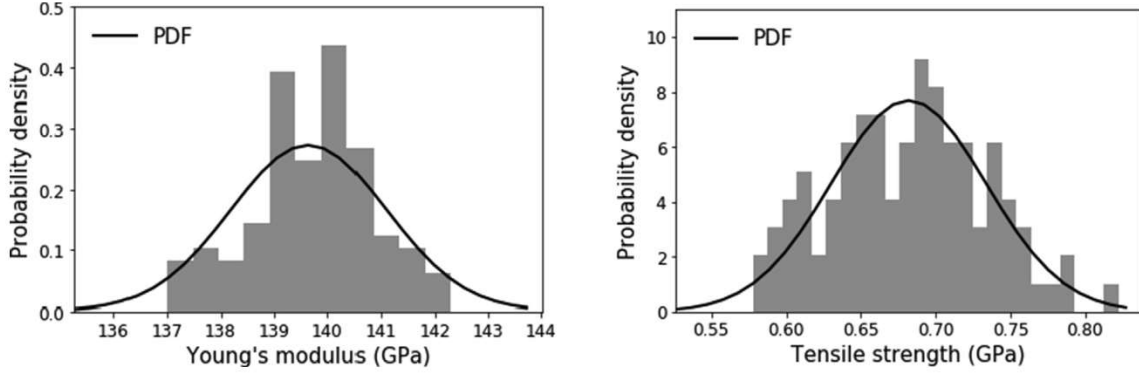
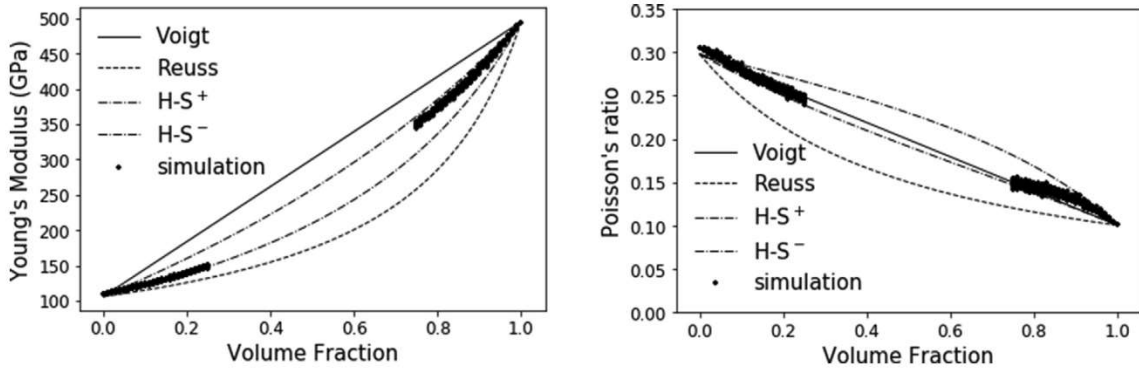
Fig. 9. Histograms of material properties of Ti-TiB₂ composites with 20% CVF.

Fig. 10. Simulated material properties compared to analytical solutions.

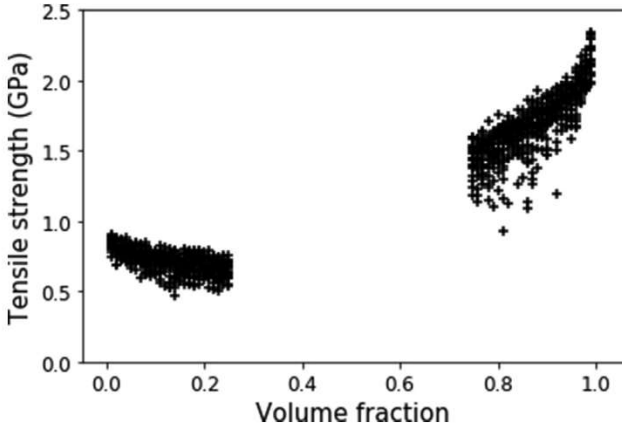


Fig. 11. Tensile strengths at various CVFs.

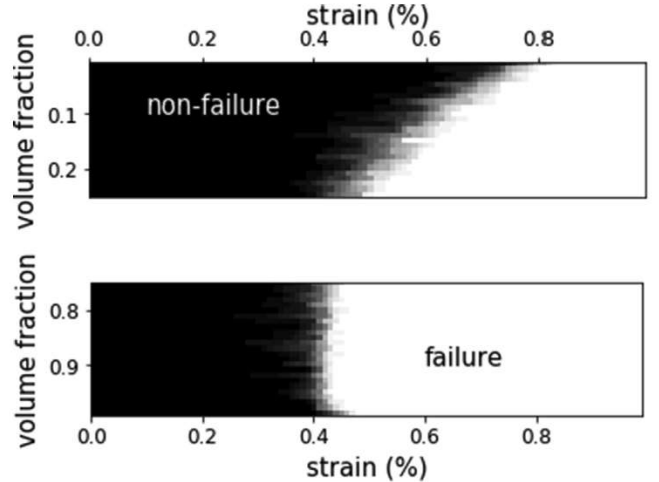


Fig. 12. A binary map representing failure/non-failure.

$$\hat{y}(\mathbf{x}) = \sum_{j=1}^N (\alpha_j - \alpha_j^*) K(\mathbf{x}_j, \mathbf{x}) + b \quad (13)$$

where N is the number of training samples, α_j and α_j^* are Lagrange multipliers, and b is the bias. K is the kernel function [65], which transforms the training data from the original input space to another feature space. There are a few optimization algorithms [63] that can be used to minimize the loss function and to generate predictive models in SVM regression. Similarly, SVMs can conduct classification [66] tasks by constructing hyperplanes in a multidimensional space that separates various labeled cases.

Gaussian process regression is a non-parametric Bayesian approach [67] to generate a model in which a wide variety of rela-

tions between inputs and outputs can be captured by utilizing a theoretically infinite number of parameters. The approximate function, $f(\mathbf{x})$, in Gaussian process regression is distributed as a Gaussian process:

$$f(\mathbf{x}) \sim \mathcal{GP}[m(\mathbf{x}), k(\mathbf{x}, \mathbf{x}')] \quad (14)$$

which is a distribution over functions and is defined by a mean and a covariance function. The mean function $m(\mathbf{x}) = E[f(\mathbf{x})]$ evaluates the average of all functions in the distribution at the input \mathbf{x} . The covariance function, $k(\mathbf{x}, \mathbf{x}') = E[(f(\mathbf{x}) - m(\mathbf{x}))(f(\mathbf{x}') - m(\mathbf{x}'))]$, repre-

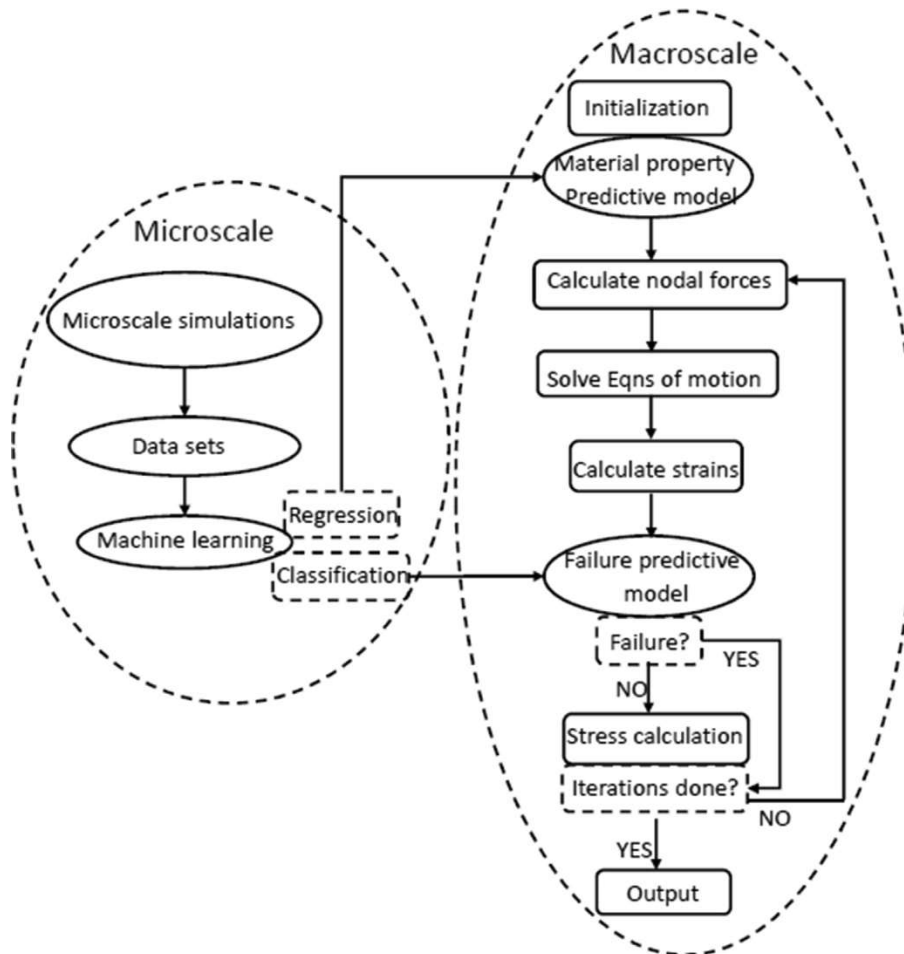


Fig. 13. A microscale/macroscopic hierarchical multiscale modeling framework.

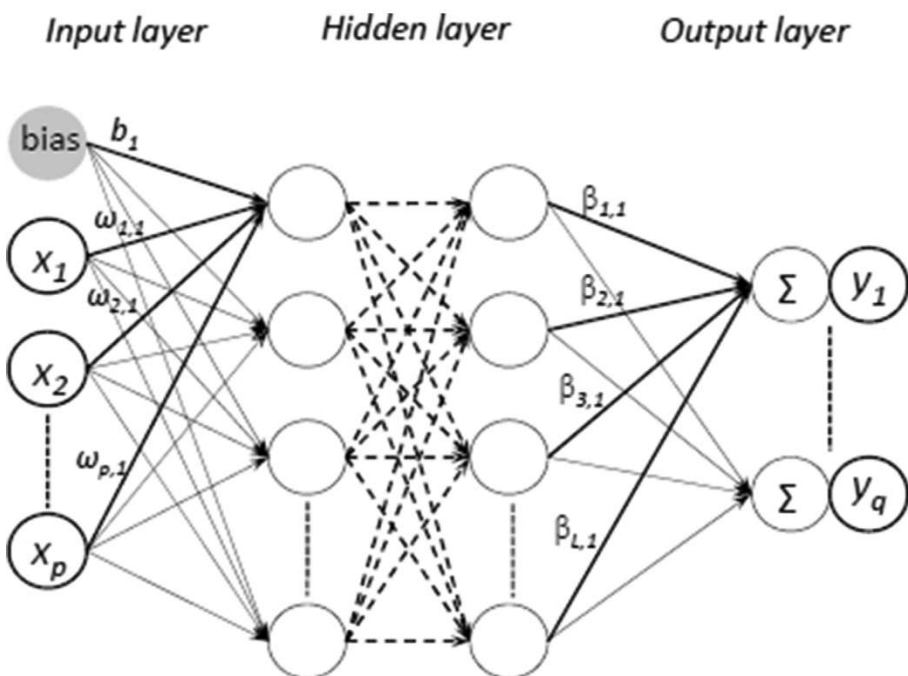


Fig. 14. An artificial neural network (ANN).

sents the dependence between the outputs at different input points \mathbf{x} and \mathbf{x}' . The covariance function serves as the kernel of the Gaussian process [68] and is chosen based on the smoothness and likely patterns to be expected in the data. In summary, the Gaussian process generates a model in which a function that infers a probability distribution over all possible values.

A fully connected ANN [69] includes an input layer, an output layer, and hidden layers, as shown in Fig. 14. During the feed-forward process, every neuron in the hidden layers transforms the outputs from the previous layer into a different representation, which is taken as the input to the next layer. There are two steps in the transformation. First, the data from the previous layer is projected into the neuron via the weights. Then, the projected data is transformed via the activation function. The backpropagation process updates the weight for the purpose of optimizing the neural network model.

4.2. Model training for regression and classification

Machine learning models play an important role in the proposed hierarchical multiscale framework to pass the information from a small scale to a large scale. In this paper, based on the collected data sets from microscale simulations, two regression models and one classification model are trained and then implemented in macroscale simulations. A data set of 1250 data samples, in which the feature is the CVF and the output targets are Young's modulus and Poisson's ratio, are used to train two regression models. One is used to predict Young's modulus according to the CVF distribution in the simulation domain, and the other is used to predict Poisson's ratio. Since Young's modulus and Poisson's ratio do not have large variabilities related to microstructure uncertainties, predictions from the regression models are deterministic. Support vector regressors (SVRs) with radial basis kernels [63] are adopted as the material property predictive models in this paper. Grid search and Five-fold cross-validation are utilized to tune hyperparameters in SVRs so that overfitting can be prevented. The normalized mean squared errors on the test set are 0.017% and 0.022%, respectively. With the predictive models, Young's modulus and Poisson's ratio for Ti-TiB₂ composites with CVFs between 26% and 74% can be estimated as well. The material property predictions, compared to the test data set and the analytical solutions, are shown in Fig. 15. We also conducted the ridge regressions, i.e., the polynomial regressions with L2 regularization, and obtained similar results. It shall be noted that polynomial curve fitting without regularization may result in overfitting, especially when more features (e.g., temperature, CVF gradient, etc.) will be considered in future work.

The data set of 1250 data samples, in which the feature is the CVF and the output target is the tensile strength, is used to train a Gaussian process regression model for the prediction of tensile strength. A Matern kernel is utilized, and the mean prediction and the 95% confidence interval are shown in Fig. 16. Fig. 16 also includes a histogram displaying the distribution of tensile strength at 40% CVF. The Gaussian process regression model can be implemented in the macroscale simulations so that the tensile strength with uncertainty distribution at each material point will be predicted at the beginning of the simulation. Our multiscale modeling uses an alternative approach via an ANN-based classification model, which directly predicts the failure probability according to the calculated strain state and the CVF at each material point.

A fully connected ANN containing three hidden layers (8, 16, 8 neurons) is trained for failure classification based on the collection of 162,500 data samples (130 data samples at different strains per simulation), in which the features are the CVF and the strain while the output is the Boolean value representing failure/non-failure. The "relu" activation function is employed in the hidden layers, while the "softmax" activation function is utilized in the output layer so that the probability can be predicted with the Boolean output. Ten-fold cross-validation is conducted, and the test score (i.e., the accuracy of the test set) is 97%. Also, the precision, recall, and F1-score are calculated as 0.98, 0.96, and 0.97, respectively. It shall be noted that the accuracy cannot reach 100% because there is no clear decision boundary between failure and non-failure domains. After the ANN is well trained, it is implemented in the macroscale simulations to estimate the failure probability instead of deterministically predicting failure or non-failure at any material point with the prescribed CVF and calculated strain. Fig. 17 shows the failure probability map generated by the ANN predictive model in the CVF-strain space. The black area indicates the failure with 0% probability, i.e., the non-failure domain, while the white area indicates the failure with 100% probability, i.e., the failure domain. The grey area at the interface of two domains represents the change of the failure probability.

As described above, we have conducted 100 microscale simulations of metal-ceramic composites with 10% CVF and another 100 simulations of composites with 20% CVF to study the variabilities of material properties due to microstructure uncertainties. It shall be noted that only the results from 50 (25 for each CVF) of those 200 simulations are included in the data sets to train and to test the neural network. To further validate the failure predictive model, we use the data samples from all of 200 simulations to calculate the failure probability of composites at the strains from 0% to 1%. It can be seen in Fig. 18 that the predictions from the neural network compare very well with the simulation results. We also use the original failure data set to train a logistic regression model

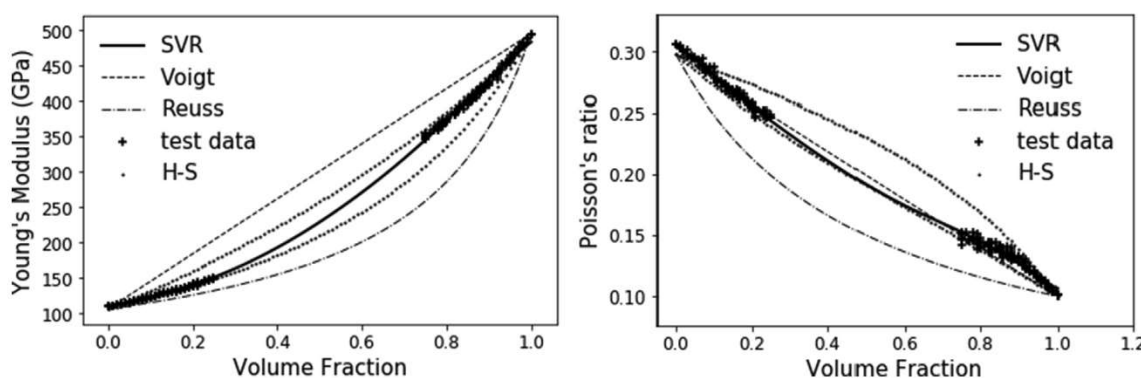
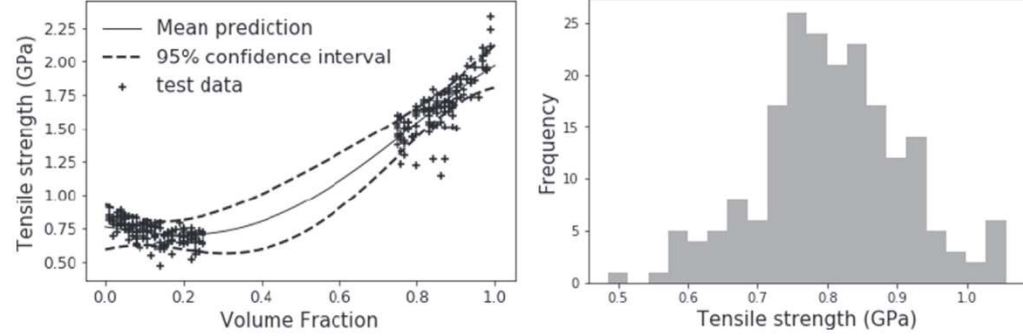


Fig. 15. Support vector regression of material properties.



(a) Mean prediction and 95% confidence interval (b) Tensile strength prediction at 40% CVF

Fig. 16. Gaussian process regression prediction.

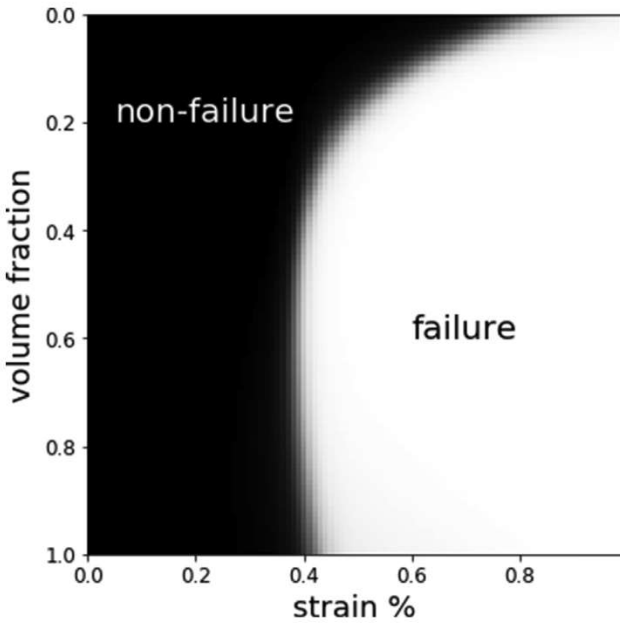


Fig. 17. Failure probability map generated via ANN classification model.

and an SVM classification model. The results from the logistic regression model are not as good as the neural network predictions. However, the SVM classification model gives similar results to the neural network.

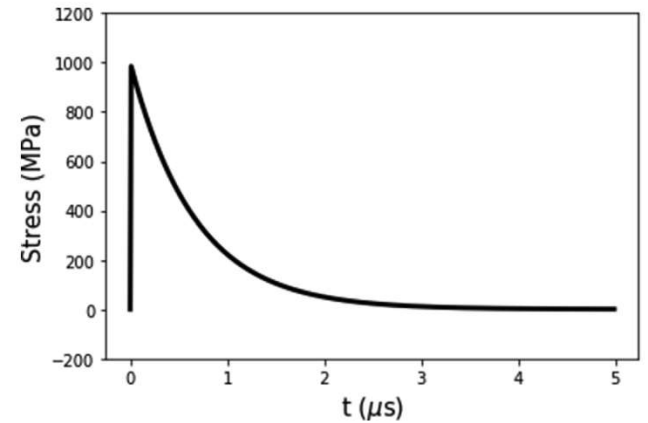


Fig. 19. A pressure pulse to approximate loading via an explosion.

5. Macroscale simulations

In macroscale finite element simulations, Young's modulus and Poisson's ratio are pre-predicted at each element according to the CVF distribution initialized in the simulation domain. The failure predictive model is implemented in the FEM simulations to predict failure probability at each element at each time step. A randomly generated number between 0 and 1, pre-assigned to each element at the beginning of each simulation, is used to determine failure or non-failure according to the predicted failure probability during the simulation.

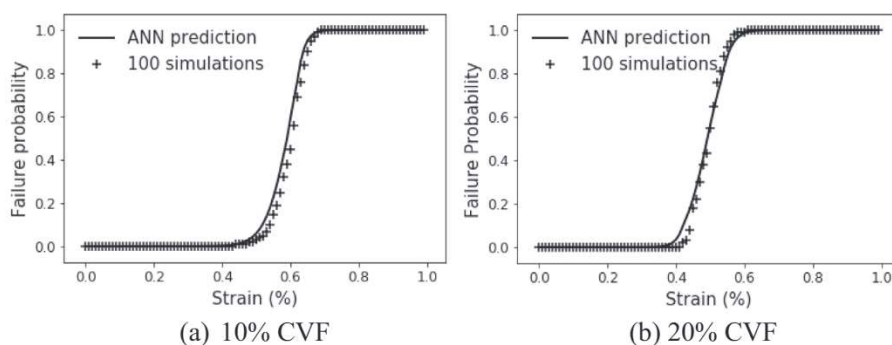


Fig. 18. Failure probability distributions.

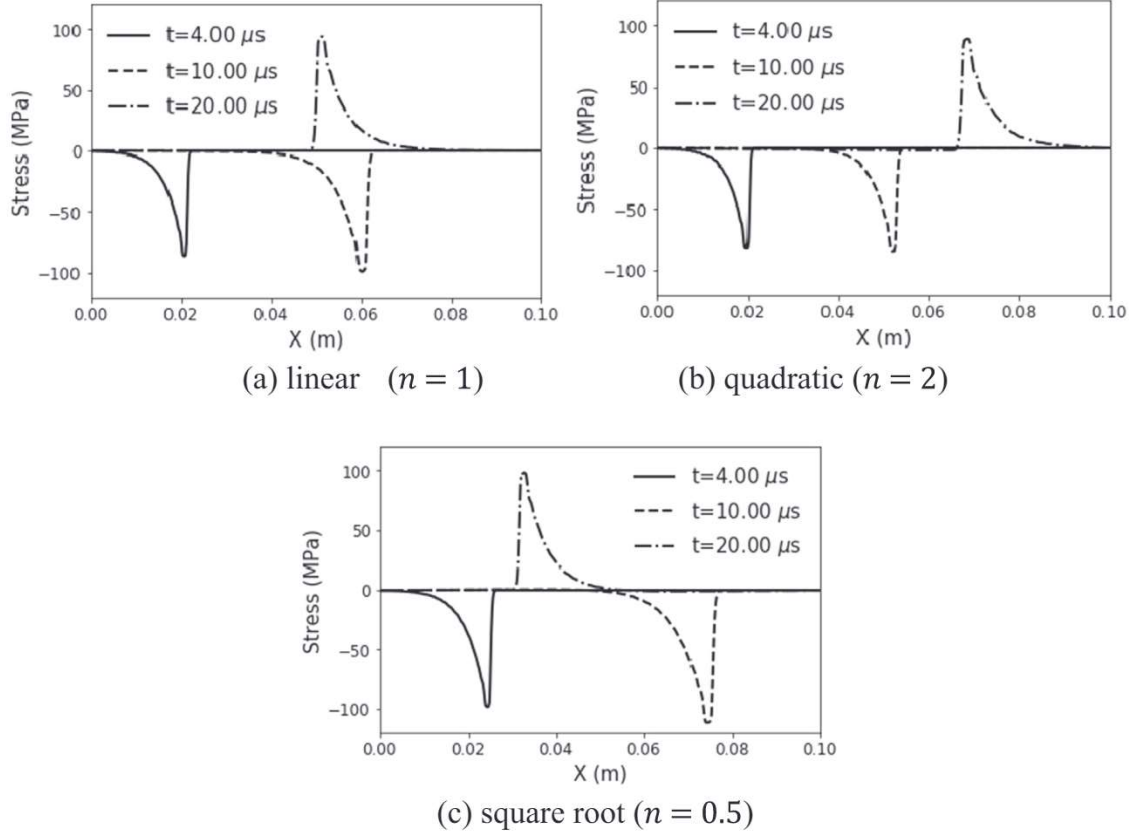


Fig. 20. Shock wave propagations along with the thickness of STM plates.

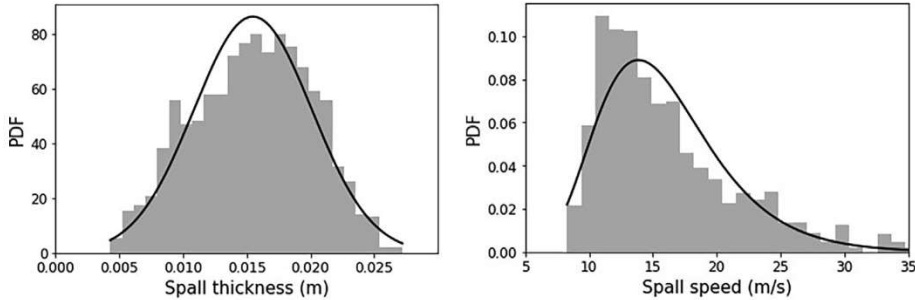


Fig. 21. Histograms of spall thickness and speed of the plate with the linear CVF distribution.

5.1. Shock wave propagation and spallation in STM plates

At first, we study the shock wave propagation and spallation in spatially tailored Ti-TiB₂ plates with a thickness of 0.1 m. The volume fraction varies along with the plate thickness. Spallation [70] is an interesting component of dynamic fracture. This phenomenon occurs when shock waves interact to produce a region of tension in the interior of a material body. The spallation usually occurs under dynamic loadings, such as impact and explosion. In this paper, a pressure pulse, described by an exponential function in Eq. (15) and shown in Fig. 19, is employed to model the explosion loaded on one surface of the plates in our simulations.

$$\sigma = \sigma_0 e^{-\beta t} \quad (15)$$

where σ_0 is the amplitude, and $\beta = -0.15e7 \text{ s}^{-1}$.

It shall be noted that the other surface of the plate is free. When the pressure pulse is applied, there is a compressive shock wave propagating along with the plate thickness. After the wave is

reflected by the free surface, the compressive shock wave becomes a tensile shock wave. It is assumed that the CVF is 0% at the loading surface and 100% at the free surface. Three types of plates with various CVF distributions are considered according to Eq. (1): linear ($n = 1$), quadratic ($n = 2$), and square root ($n = 0.5$), as depicted in Figs. 1 and 2.

A pressure pulse with the amplitude of $\sigma_0 = 100 \text{ MPa}$ is employed first to study shock wave propagation along with the thickness of the Ti-TiB₂ plates. A one-dimensional FEM model with two-node bar elements is adopted with the flux-corrected transport (FCT) algorithm [70–72] to maintain the strong discontinuity at the shock wavefronts. Fig. 20 shows the shock wave propagation profiles at different times. According to Eq. (1) and Fig. 1, the CVF rapidly changes with a square root distribution and slowly changes with a quadratic distribution in comparison to the linear CVF distribution. Young's modulus follows the same trends as predicted by the regression model (shown in Fig. 15). As a result, the shock wave propagates faster in the plate with a square root CVF distri-

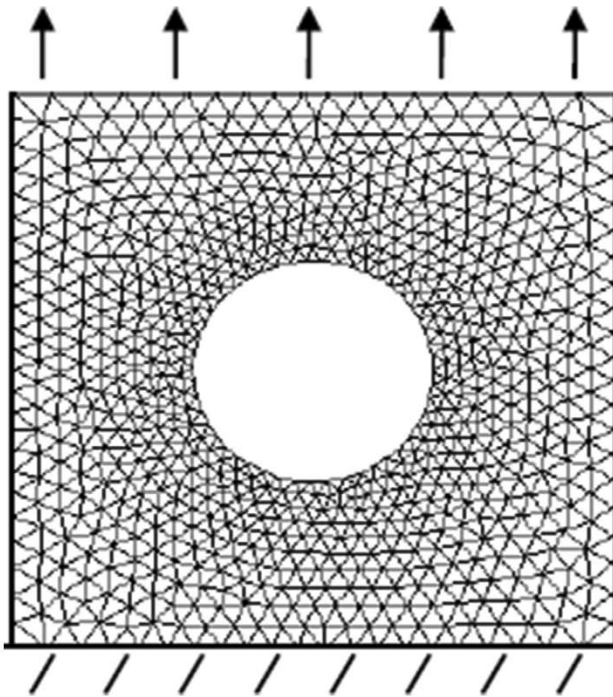


Fig. 22. An STM plate with a central hole subjected to a tensile stress.

bution and slower in the plate with a quadratic CVF distribution, compared to the shock wave propagating in the plate with a linear CVF distribution. This phenomenon can be observed in Fig. 20. Correspondingly, the changes in shock wave amplitude vary because the unloading wave speeds are different at the plates with different CVF distributions.

If the amplitude of a pressure pulse is high enough, it is possible that the spallation occurs once a non-zero failure probability is predicted via the ANN classification model. We consider another pressure pulse with an amplitude of 650 MPa, and 300 simulations are conducted for each plate. We find that no spallation is observed in the plate with a quadratic CVF distribution but that it is observed in the other two plates. According to the simulation results, it can be concluded that the reliability of the plate with a linear CVF distribution under the pressure pulse with an amplitude of 650 MPa is calculated as 93.3%, while the reliability of the plate with a square root CVF distribution is 96.7%.

When the amplitude of the pressure pulse is increased to 1200 MPa, the spallation occurs in all simulations. The calculated spall thickness and speed are random variables because of the failure probability due to microstructure uncertainties. We first analyze the collected data based on 1000 simulations of the plates with the linear CVF distribution. The histograms in Fig. 21 demonstrate that the spall thickness follows the normal distribution while the spall speed follows the log-normal distribution. In summary, Table 2 includes the calculated means and standard deviations of the spall thicknesses and the modes of the spall speeds for all three plates. It can be seen that the plate with a quadratic CVF distribution has the smallest mean spall thickness and the

highest mean spall speed, while the plate with a square root CVF distribution has the largest mean spall thickness and the lowest mean spall speed.

5.2. Failure probability profiles in central-holed plates

Another example we study includes 5 mm × 5 mm Ti-TiB₂ plates with a central hole subjected to a tensile stress of 300 MPa on the top surface as shown in Fig. 22. Two-dimensional finite element analyses with plane stress states are conducted. Triangular elements are employed. According to Eq. (2), there are four control parameters for the CVF distribution: η_x , η_z , n_x , and n_z , in addition to $\nu_0 = 0\%$ and $\nu_1 = 100\%$. We consider three plates with different CVF distributions and compare the failure probability profiles after the tensile stress is applied for 1.5 ms. It shall be noted that the principal strain is calculated at each element for failure prediction. The failure probability profiles in Fig. 23 show that the failure would occur at the stress concentration regions (i.e., around the hole) but most likely in the regions with smaller CVFs.

6. Conclusions and future outlook

In this paper, we propose a hierarchical multiscale method in which machine learning (ML) plays an important role in bridging microscale and macroscale. The multiscale framework includes conducting microscale simulations to generate data sets, which are used to train ML regression and classification models. Then, well-trained ML models are implemented in macroscale simulations. We utilize this hierarchical multiscale method to study metal-ceramic spatially tailored materials (STMs), in which the volume fraction varies in space at the macroscale. Microstructure uncertainties are considered when generating sample configurations for microscale simulations. It is observed that the material properties, including Young's modulus and Poisson's ratio, have small variabilities but that the failure strength has a large variability. Based on the collected data sets, two support vector machines (SVMs) are trained to predict material properties (i.e., Young's modulus and Poisson's ratio). In addition, an artificial neural network (ANN) is trained to predict the material failure probability at the location with a prescribed ceramic volume fraction and the calculated strain during the simulation. Those learning machines are then implemented in macroscale simulations to study mechanical behaviors of STM-based plates under various loading conditions.

The challenges of the proposed method include learning machine selection and dataset optimization. It is challenging to select the "right" type of learning machines to conduct relevant data analyses. In this paper, metal-ceramic STMs mostly exhibit linear elasticity with small deformations. Therefore, simply predicting material properties is sufficient to pass the information from microscale to macroscale. If microscale mechanical responses are nonlinear, learning machines to approximate the stress-strain relationship would be needed. Moreover, if mechanical responses are rate-dependent, a recurrent neural network (RNN) might be a better choice. An alternative solution could be adding strains at previous time steps as additional features if a fully connected feed-forward neural network is used. On the other hand, Bayesian ML

Table 2
Spall thickness and spall speed.

	Plates with a linear CVF distribution	Plates with a quadratic CVF distribution	Plates with a square root CVF distribution
Spall thickness (m)	0.0155 ± 0.0046	0.0121 ± 0.0026	0.0175 ± 0.0070
Spall speed mode (m/s)	13.87	17.89	10.83

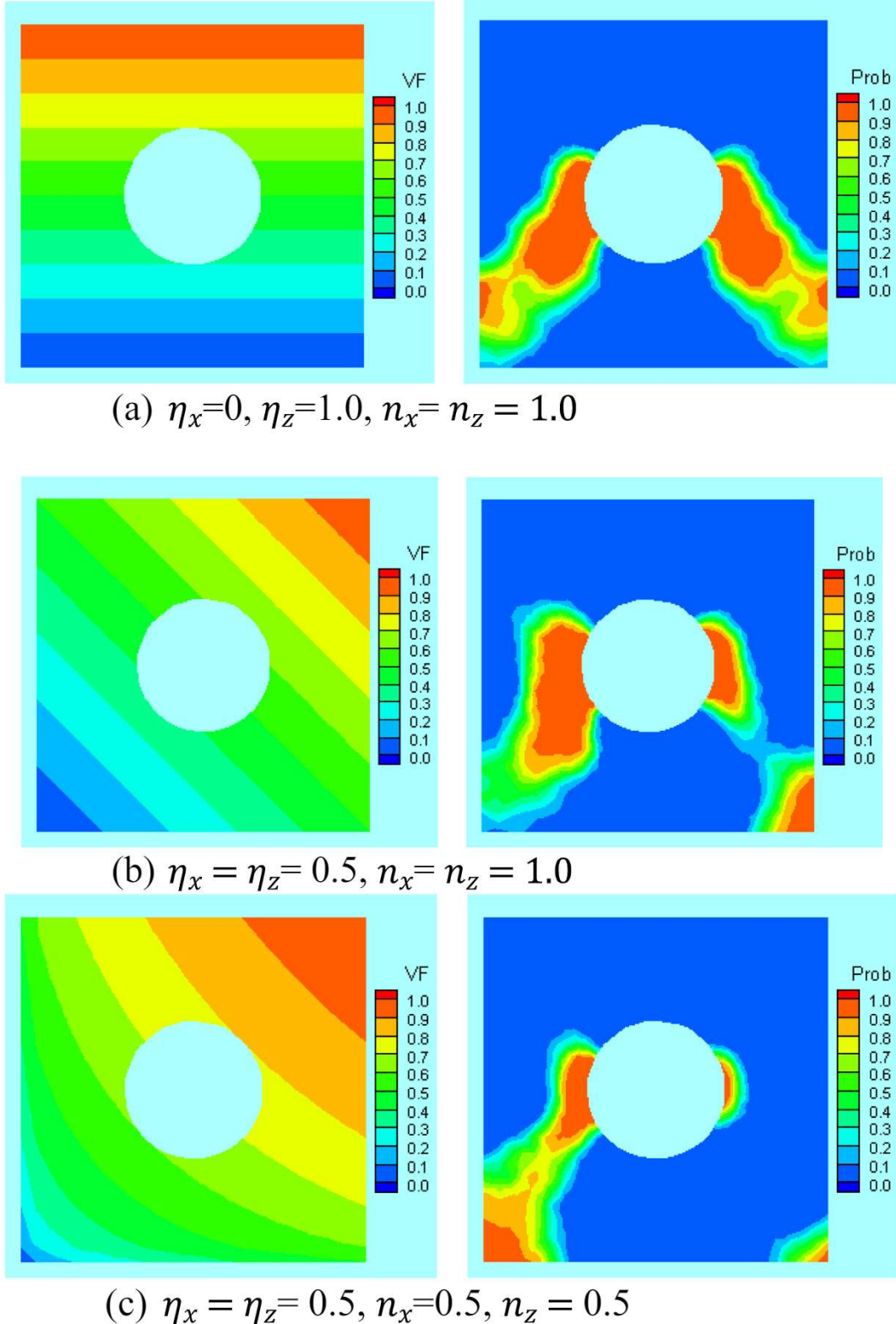


Fig. 23. In-plane CVF distributions (left) and the failure probability profiles (right).

models need to be considered in the future for material failure probability prediction. Another challenge is how to perform optimal sampling so that the collected data sets contain the data samples with high importance. The sensitivity of the data samples needs to be studied in order to reduce the number of microscale simulations and avoid generating unnecessary data samples.

Our microstructure model of metal-ceramic STMs can be improved in future studies by considering clusters so that micro-scale simulations at the CVFs between 26% and 74% will be conducted. There is an assumption of perfect bonding between two materials in our work, and no defects (e.g., vacancy or grain boundary) are considered. Future studies will consider the interfacial

interaction mechanism between Ti(Ti-6Al-4V) and TiB₂ as well as various types of defects. Indeed, MD modeling and simulation is a good approach to study the interfacial behavior in composite materials at the nanoscale. The generated information can be passed to the microscale via ML. However, accurate potential functions of boron (B) and its compounds need to be developed (some of them are not available in the literature) before studying Ti-TiB₂ STMs at the nanoscale. In addition, it's worth mentioning that this research can be extended to studying the effect of microstructure uncertainties on multiscale damage initiation and propagation in heterogeneous composites [76,77] via the model reduction order technique [78,79].

Declaration of Competing Interest

The authors declare that they have no known competing financial interests or personal relationships that could have appeared to influence the work reported in this paper.

Acknowledgment

This research has been funded by the University of Iowa Technology Institute (formerly CCAD) Research Initiative Seed Program.

References:

- [1] Butler KT, Davies DW, Cartwright H, Isayev O, Walsh A. Machine learning for molecular and materials science. *Nature* 2018;559(7715):547–55.
- [2] Behler J. Perspective: Machine learning potentials for atomistic simulations. *J Chem Phys* 2016;145(17):219901.
- [3] Stoffel M, Bamer F, Markert B. Artificial neural networks and intelligent finite elements in non-linear structural mechanics. *Thin-Walled Struct* 2018;131:102–6.
- [4] Stoffel M, Bamer F, Markert B. Neural network based constitutive modeling of nonlinear viscoplastic structural response. *Mech Res Commun* 2019;95:85–8.
- [5] Singh K, Rajput SK, Mehta Y. Modeling of the hot deformation behavior of a high phosphorus steel using artificial neural networks. *Mater Discov* 2016;6:1–8.
- [6] Akbari Z, Mirzadeh H, Cabrera J-M. A simple constitutive model for predicting flow stress of medium carbon microalloyed steel during hot deformation. *Mater Des* 2015;77:126–31.
- [7] Sabokpa O, Zarei-Hanzaki A, Abedi HR, Haghdi N. Artificial neural network modeling to predict the high temperature flow behavior of an AZ81 magnesium alloy. *Mater Des* 2012;39:390–6.
- [8] Freitag S, Graf W, Kaliske M. A material description based on recurrent neural networks for fuzzy data and its application within the finite element method. *Comput Struct* 2013;124:29–37.
- [9] Oishi A, Yagawa G. Computational mechanics enhanced by deep learning. *Comput Methods Appl Mech Eng* 2017;327:327–51.
- [10] Meister F, Passerini T, Mihailev F, Tuysuzoglu A, Maier A, Mansi T. Deep learning acceleration of Total Lagrangian Explicit Dynamics for soft tissue mechanics. *Comput Methods Appl Mech Eng* 2020;358:112628.
- [11] Finol D, Lu Y, Mahadevan V, Srivastava A. Deep convolutional neural networks for eigenvalue problems in mechanics. *Int J Numer Methods Eng* 2019;118(5):258–75.
- [12] Capuano G, Rimoli J. Smart finite elements: A novel machine learning application. *Comput Methods Appl Mech Eng* 2019;345:363–81.
- [13] Li H et al. Clustering discretization methods for generation of material performance databases in machine learning and design optimization. *Comput Mech* 2019;64(2):281–305.
- [14] Esmailzadeh M, Aghaei-Khafri M. Finite element and artificial neural network analysis of ECAP. *Comput Mater Sci* 2012;63:127–33.
- [15] Fu Z, Mo J, Chen L, Chen W. Using genetic algorithm-back propagation neural network prediction and finite-element model simulation to optimize the process of multiple-step incremental air-bending forming of sheet metal. *Mater Des* 2010;31(1):267–77.
- [16] PourAsabi H, PourAsabi H, AmirZadeh Z, BabaZadeh M. Development a multi-layer perceptron artificial neural network model to estimate the Vickers hardness of Mn-Ni-Cu-Mo austempered ductile iron. *Mater Des* 2012;35:782–9.
- [17] Kappatos V, Chamos AN, Pantelakis SG. Assessment of the effect of existing corrosion on the tensile behaviour of magnesium alloy AZ31 using neural networks. *Mater Des* 2010;31(1):336–42.
- [18] Birbilis N, Cavanaugh MK, Sudholz AD, Zhu SM, Easton MA, Gibson MA. A combined neural network and mechanistic approach for the prediction of corrosion rate and yield strength of magnesium-rare earth alloys. *Corros Sci* 2011;53(1):168–76.
- [19] Antonescu C, Atroshchenko E, Alajlan N, Rabczuk T. Artificial neural network methods for the solution of second order boundary value problems. *Comput Mater Contin* 2019;59(1):345–59.
- [20] Samaniego E et al. An energy approach to the solution of partial differential equations in computational mechanics via machine learning: Concepts, implementation and applications. *Comput Methods Appl Mech Eng* 2020;362:112790.
- [21] Belytschko T, Xiao SP. Coupling methods for continuum model with molecular model. *Int J Multiscale Comput Eng* 2003;1(1):12.
- [22] Xiao SP, Belytschko T. A bridging domain method for coupling continua with molecular dynamics. *Comput Methods Appl Mech Eng* 2004;193(17–20):1645–69.
- [23] Xiao S, Hou W. Multiscale modeling and simulation of nanotube-based torsional oscillators. *Nanoscale Res Lett* 2007;2:54–9.
- [24] Xiao S, Hou W. Studies of nanotube-based aluminum composites using the bridging domain coupling method. *Int J Multiscale Comput Eng* 2007;5(6):447–59.
- [25] Erickson JL. The cauchy and born hypotheses for crystals. In: Phase transformations and material instabilities in solids. Elsevier; 1984. p. 61–77.
- [26] Tadmor E, Phillips R, Ortiz M. Hierarchical modeling in the mechanics of materials. *Int J Solids Struct* 2000;37(1–2):379–89.
- [27] Arroyo M, Belytschko T. A finite deformation membrane based on inter-atomic potentials for the transverse mechanics of nanotubes. *Mech Mater* 2003;35(3–6):193–215.
- [28] Xiao S, Yang W. Temperature-related Cauchy-Born rule for multiscale modeling of crystalline solids. *Comput Mater Sci* 2006;37(3):374–9.
- [29] Xiao S, Yang W. A temperature-related homogenization technique and its implementation in the meshfree particle method for nanoscale simulations. *Int J Numer Methods Eng* 2007;69(10):2099–125.
- [30] Yang W, Xiao S. Extension of the temperature-related Cauchy-Born rule: Material stability analysis and thermo-mechanical coupling. *Comput Mater Sci* 2008;41(4):431–9.
- [31] Gaffari MA, Zhang Y, Xiao SP. Molecular dynamics modeling and simulation of lubricant between sliding solids. *J Micromechanics Mol Phys* 2017;2(2):1750009.
- [32] Gaffari MA, Zhang Y, Xiao S. Multiscale modeling and simulation of rolling contact fatigue. *Int J Fatigue* 2018;108:9–17.
- [33] Jiang S, Tao J, Sewell TD, Chen Z. Hierarchical multiscale simulations of crystalline β -octahydro-1,3,5,7-tetranitro-1,3,5,7-tetrazocine (β -HMX): Generalized interpolation material point method simulations of brittle fracture using an elastodamage model derived from molecular dynamics. *Int J Damage Mech* 2017;26(2):293–313.
- [34] Alber M et al. Integrating machine learning and multiscale modeling—perspectives, challenges, and opportunities in the biological, biomedical, and behavioral sciences. *npj Digit Med* 2019;2(1):115.
- [35] Unger JF, Könke C. Neural networks as material models within a multiscale approach. *Comput Struct* 2009;87(19–20):1177–86.
- [36] Liu Z, Wu CT, Koishi M. A deep material network for multiscale topology learning and accelerated nonlinear modeling of heterogeneous materials. *Comput Methods Appl Mech Eng* 2019;345:1138–68.
- [37] White DA, Arrighi WJ, Kudo J, Watts SE. Multiscale topology optimization using neural network surrogate models. *Comput Methods Appl Mech Eng* 2019;346:1118–35.
- [38] Lu C, Sambasivan S, Kapahi A, Udaykumar HS. Multi-scale modeling of shock interaction with a cloud of particles using an artificial neural network for model representation. *Procedia IUTAM* 2012;3:25–52.
- [39] Xiao S, Hu R, Li Z, Attarian S, Björk K-M, Lendasse A. A machine-learning-enhanced hierarchical multiscale method for bridging from molecular dynamics to continua. *Neural Comput Appl* 2019;9:1–15.
- [40] Wang K, Sun WC. A multiscale multi-permeability poroplasticity model linked by recursive homogenizations and deep learning. *Comput Methods Appl Mech Eng* 2018;334:337–80.
- [41] Liu Z, Wu CT. Exploring the 3D architectures of deep material network in data-driven multiscale mechanics. *J Mech Phys Solids* 2019;127:20–46.
- [42] Balokas G, Czichon S, Rolfs R. Neural network assisted multiscale analysis for the elastic properties prediction of 3D braided composites under uncertainty. *Compos Struct* 2018;183:550–62.
- [43] Birman V, Chona R, Byrd LW, Haney MA. Response of spatially tailored structures to thermal loading. *J Eng Math* 2008;61(2–4):201–17.
- [44] Patil AS, Hiwarkar VD, Verma PK, Khatirkar RK. Effect of TiB₂ addition on the microstructure and wear resistance of Ti-6Al-4V alloy fabricated through direct metal laser sintering (DMLS). *J Alloys Compd* 2019;777:165–73.
- [45] Shishkovsky I, Kovakina N, Sherbakov V. Graded layered titanium composite structures with TiB₂ inclusions fabricated by selective laser melting. *Compos Struct* 2017;169:90–6.
- [46] Cai C et al. In-situ preparation and formation of TiB/Ti-6Al-4V nanocomposite via laser additive manufacturing: Microstructure evolution and tribological behavior. *Powder Technol* 2019;342:73–84.
- [47] Moulinec H, Suquet P. Comparison of FFT-based methods for computing the response of composites with highly contrasted mechanical properties. *Phys B Condens Matter* 2003;338(1–4):58–60.

- [48] Segurado J, Llorca J. A numerical approximation to the elastic properties of sphere-reinforced composites. *J Mech Phys Solids* 2002;50(10):2107–21.
- [49] Ghossein E, Lévesque M. A fully automated numerical tool for a comprehensive validation of homogenization models and its application to spherical particles reinforced composites. *Int J Solids Struct* 2012;49(11–12):1387–98.
- [50] Deierling PE, Zhupanska OI. Computational modeling of the effective properties of spatially graded composites. *Int J Mech Sci* 2018;145:145–57.
- [51] Xiao S, Lendasse A, Hu R. Data-enabled computational multiscale method in materials science and engineering. Proceedings – 2018 international conference on Computational Science and Computational Intelligence (CSCI), 2018.
- [52] W. American Society for Metals. Properties and selection–nonferrous alloys and pure metals, 9 ed., 1. Metals Park Ohio: American Society for Metals; 1979.
- [53] Munro RG. Material properties of titanium diboride. *J Res Natl Inst Stand Technol* 2000;105(5):709–20.
- [54] Wiley DE, Manning WR, Hunter O. Elastic properties of polycrystalline TiB₂, ZrB₂ and HfB₂ from room temperature to 1300 °K. *J Less Common Met* 1969;18(2):149–57.
- [55] Xiao S, Wang S, Ni J, Briggs R, Rysz M. Reliability analysis of carbon nanotubes using molecular dynamics with the aid of grid computing. *J Comput Theor Nanosci* 2008;5(4):528–34.
- [56] Ma J, He Z, Tan GEB. Fabrication and characterization of Ti-TiB₂ functionally graded material system. *Metall Mater Trans A* 2002;33(3):681–5.
- [57] Anandajothi M, Ramanathan S, Ananthi V, Narayanasamy P. Fabrication and characterization of Ti6Al4V/TiB₂-TiC composites by powder metallurgy method. *Rare Met* 2017;36(10):806–11.
- [58] Belytschko T, Liu WK, Moran B. Nonlinear finite elements for continua and structures. Wiley; 2000.
- [59] Voigt W. Theoretische Studien über die Elastizitätsverhältnisse der Krystalle. I. Abhandlungen der Königlichen Gesellschaft der Wissenschaften Göttingen 1887;34:3–52.
- [60] Reuss A. Berechnung der Fließgrenze von Mischkristallen auf Grund der Plastizitätsbedingung für Einkristalle. *ZAMM – J Appl Math Mech/Zeitschrift für Angew Math und Mech* 1929;9(1):49–58.
- [61] Hashin Z, Shtrikman S. A variational approach to the theory of the elastic behaviour of multiphase materials. *J Mech Phys Solids* 1963;11(2):127–40.
- [62] Vapnik VN. The nature of statistical learning theory. New York, NY: Springer, New York; 2000.
- [63] Smola Aj, Schölkopf B. A tutorial on support vector regression. *Stat Comput* 2004;14(3):199–222.
- [64] Hsu C-W, Lin C-J. A comparison of methods for multiclass support vector machines. *IEEE Trans Neural Networks* 2002;13(2):415–25.
- [65] Chang Y et al. Training and testing low-degree polynomial data mappings via linear svm. *J Mach Learn Res* 2010;11:1471–90.
- [66] Foody GM, Mathur A. Toward intelligent training of supervised image classifications: Directing training data acquisition for SVM classification. *Remote Sens Environ* 2004;93(1–2):107–17.
- [67] Gershman SJ, Blei DM. A tutorial on Bayesian nonparametric models. *J Math Psychol* 2012;56(1):1–12.
- [68] Jäkel F, Schölkopf B, Wichmann FA. A tutorial on kernel methods for categorization. *J Math Psychol* 2007;51(6):343–58.
- [69] Dreiseitl S, Ohno-Machado L. Logistic regression and artificial neural network classification models: A methodology review. *J Biomed Inform* 2002;35(5–6):352–9.
- [70] Xiao S. A non-oscillatory method for spallation studies. *Int J Numer Methods Eng* 2006;66:364–80.
- [71] Xiao S. An FE-FCT method with implicit functions for the study of shock wave propagation in solids. *Wave Motion* 2004;40(3):263–76.
- [72] Xiao S. A lattice Boltzmann method for shock wave propagation in solids. *Commun Numer Methods Eng* 2006;23(1):71–84.
- [73] Talebi H, Silani M, Bordas SPA, Kerfriden P, Rabczuk T. Molecular dynamics/xfem coupling by a three-dimensional extended bridging domain with applications to dynamic brittle fracture. *Int J Multiscale Comput Eng* 2013;11(6):527–41.
- [74] Talebi H, Silani M, Bordas SPA, Kerfriden P, Rabczuk T. A computational library for multiscale modeling of material failure. *Comput Mech* 2014;53(5):1047–71.
- [75] Silani M, Ziae Rad S, Talebi H, Rabczuk T. A semi-concurrent multiscale approach for modeling damage in nanocomposites. *Theor Appl Frac Mech* 2014;74(1):30–8.
- [76] Dunant CF, Bordas SPA, Kerfriden P, Scrivener KL, Rabczuk T. An algorithm to compute damage from load in composites. *Front Archit Civ Eng China* 2011;5(2):180–93.
- [77] Akbari Rahimabadi A, Kerfriden P, Bordas SPA. Scale selection in nonlinear fracture mechanics of heterogeneous materials. *Philos Mag* 2015;95(28–30):3328–47.
- [78] Kerfriden P, Passieux JC, Bordas SPA. Local/global model order reduction strategy for the simulation of quasi-brittle fracture. *Int J Numer Methods Eng* 2012;89(2):154–79.
- [79] Hoang KC, Kerfriden P, Bordas SPA. A fast, certified and ‘tuning free’ two-field reduced basis method for the metamodeling of affinely-parametrised elasticity problems. *Comput Methods Appl Mech Eng* 2016;298:121–58.